

UNIVERSIDAD DE SALAMANCA

FACULTAD DE CIENCIAS

DEPARTAMENTO DE FISICA

MASTER EN FISICA Y TECNOLOGIA DE LOS LASERES



# **Experimental characterization of nanodevices based on graphene on hexagonal boron nitride**

Paolo Pedrinazzi

**Tutor**

Doc. E. Diez Fernandez

a.a. 2012-2013



# Contents

## Contents

1	Summary	4
2	Introduction	6
3	Optical characterization	11
4	Raman Spectroscopy	18
5	Electronic properties	28
6	Magnetotransport experiments	36
7	Conclusions	50
	Bibliography	52

# 1. Summary

Graphene is the first truly 2D system that can be studied. Since its discovery in 2004, it has been studied by many research groups and a lot of discoveries were done. In this moment many groups are still interested in graphene and they go on studying it. Until 2010 graphene was studied deposited on Si/SiO<sub>2</sub> substrates: its properties were not the expected ones because the mobility value was affected by the presence of the substrate and its interactions with the graphene flake. During these years, graphene of the highest quality was the suspended one: exfoliated a flake on the SiO<sub>2</sub>, the part down to the graphene was quit chemically leaving only two edges on the oxide. In 2010 hexagonal boron nitride (h-BN), produced in large single crystals, was utilized in this field: graphene properties were enhanced thanks to the low interaction with the h-BN substrate.

In the first part of this work we will provide an introductory overview on graphene and on hexagonal boron nitride. This includes a brief introduction on both graphene and h-BN, having a look on the historical point of view and a qualitative discussion on them. Subsequently we will treat graphene's electronic and optical properties, as introduction to the experimental results of the next part of the work. This introduction on the properties is important because the theories and the properties we will use are derived from them.

In the second part of our work we will present the results of our measurements, taken in the three months between February and May. We took Raman and magnetotransport measurements respectively at the Department of Physics of Pavia (under the tutorship of Prof. Vittorio Bellani) and at the Low Temperature Laboratory

of Salamanca (under the tutorship of Doc. Enrique Diez). We applied Raman spectroscopy to graphene and h-BN flakes exfoliated on Si/SiO<sub>2</sub> substrates for a first characterization, while in Salamanca we worked on a single sample of MLG deposited on h-BN and on SiO<sub>2</sub>. All the results reported are taken from magnetotransport measurements of this sample at low temperature ( $\sim 300mK$ ). We will introduce the theories that we tried to apply to understand the behavior of this sample, characterized by large inhomogeneity. In my opinion the work is really interesting because during this project we learned and improved the production process of the samples, in order to optimize the work with the instruments present in our laboratory. The purpose is to begin a work that will be developed and continued in the future, probably employing also CVD graphene.

## 2. Introduction

“Carbon is the materia prima for life in the planet and the basis of all organic chemistry”. (Castro Neto, [1])

Carbon, which has Atomic Number  $Z=6$  and characterized by the electronic series  $1s^2 2s^2 2p^2$ , is peculiar for life and for nature thanks to the ways it can aggregate: the allotropes. Allotropes are due to the hybridization of the electronic orbitals  $s$  and  $p$  that bound carbon atoms with covalent bonds to form systems with different dimensionality.

The crystal structures they form are different, depending on the type of hybridization. Graphene is the 2D allotrope of carbon, recently produced and very important to understand physical and electrical quantum properties. It is made out of carbon atoms arranged on a honeycomb (hexagonal) structure, like benzene rings without hydrogens. Carbons arrange in this structure by its  $sp^2$  atomic hybridization. The oldest C-allotrope known was graphite by the invention of the pencil in 1564: this is the 3D crystal allotrope of carbon (due to the  $sp^3$  hybridization of C atoms), used mainly as an instrument of writing thanks to the fact that it is made out of stacks of graphene layers weakly coupled by van der Waals forces. When the tip of the pencil is pressed on the surface of a paper sheet, it is producing graphene sheets breaking these Van der Waals bonds. Other important allotropes are fullerenes, molecules where carbon atoms are arranged spherically. From the physical point of view are quasi-0D objects with discrete energy states. They can be ideally obtained from graphene introducing pentagon structures that produce defects of positive curvature, forcing the graphene sheet to wrap up itself. One of the most important fullerenes is the Fullerene C60,

famous for its form of truncated icosahedron and discovered in the 1985. It is possible to produce also the 1D allotrope of carbon, called carbon nanotube, by rolling a graphene sheet along a given direction and re-bonding C-C atoms. They have a metallic or semiconducting behavior, depending on the rolling direction of graphene.

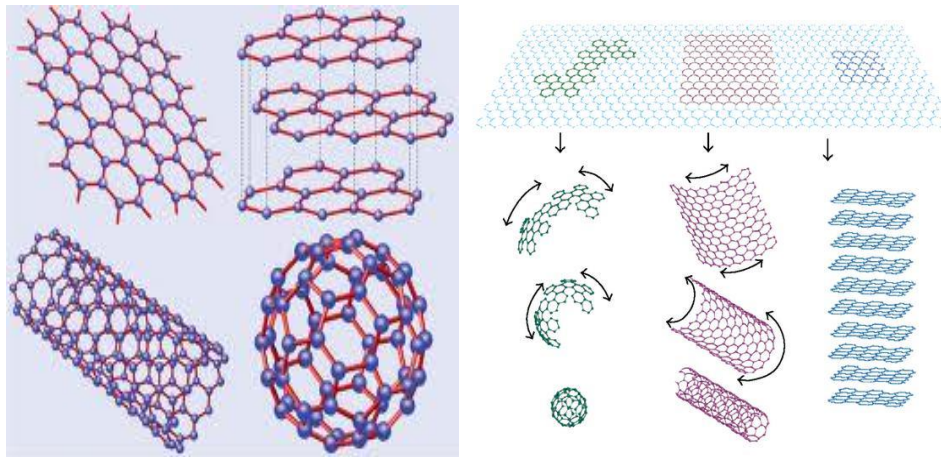


**Figure 1.** In the left picture we can see a graphene 2D plane, a graphene stacking (graphite), a carbon nanotube and a fullerene molecule. In the second one (right) it is shown how, from graphene, it is possible to build C-allotropes.

Graphene is essentially the base of all these allotropes (see *Figure 1.*). In particular there's not a limit in the number of layers connected together: there are mono-Layer graphene (MLG), bi-layer graphene (BLG), tri-layer graphene (TLG) and the multilayers, like graphite. There's not a severe distinction on the dimensionality, in particular MLG, BLG and TLG are studied as 2D materials for their exceptional electronic properties.

Since the beginning of the 20<sup>th</sup> Century graphene's properties were studied theoretically. In 1947 P. R. Wallace published a theoretical work in which were derived graphene's peculiar energy dispersion relations, obtained via tight-binding calculation. At this time was universally thought impossible to produce a pure 2-D material like graphene because of its high instability: in fact at any finite temperature a divergent

contribution of thermal fluctuations should prevent it to stand alone. This idea was unexpectedly changed when, in 2004, A. Geim, K. M. Novoselov and their Manchester's group produced the first flakes of mono-layer graphene. Surprisingly, the production technique used was really simple: they mechanically exfoliated graphite with a common scotch tape, performing a repeated peeling. The existence of this 2D material is due to the presence of a substrate: applying the scotch to the surface of the Si/SiO<sub>2</sub> substrate with a gentle pressure, it is possible to transfer pieces and flakes of graphene of different number of layers and dimension. In particular is the silicon oxide insulating substrate that gives an intrinsic stability in the third dimension, giving graphene the possibility to exist at finite temperature. This stability is granted by bonds between the flake and the substrate; this is reflected also in the presence of fluctuations in the planarity of graphene, as could be seen in the simulation of *Figure 2.*

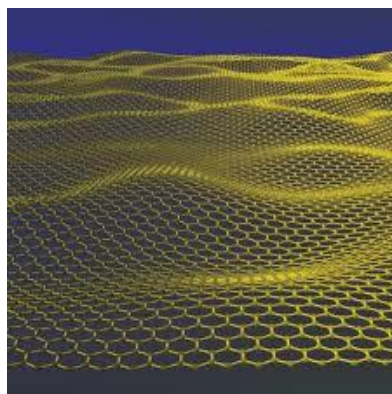


**Figure 2.** Surface fluctuations in graphene.

Although it should seem a drastic and time consuming technique, the mechanical exfoliation is the best way to produce high pure graphene sheets. In my experience, the layers are rare and small, more or less tens of  $\mu m$  sized, but with optimal electronic characteristic. There are other ways to produce graphene: a lot of people try to produce larger sized graphene sheet for industrial applications, with the goal of

increasing its electronic qualities. Nowadays one of the most interesting way is the Chemically Vapor Deposition (CVD graphene). It hasn't got a good quantum quality and now shouldn't be employed for fundamental quantum property research but researchers and firms are developing the system to produce it: in the future should be the right idea for industrial large scale application.

An evolution of the scotch tape technique is to deposit graphene on the silicon oxide substrate and with chemical etching remove the  $\text{SiO}_2$  under the graphene layer: it remains suspended between two sides, so its electrical properties and its purity should be enhanced. The problem of this technique is that these flakes are really delicate and easy to be broken.

In these last years the most "simple" and secure way to produce ultra-high pure graphene is to mechanically exfoliate hexagonal Boron Nitride on Si/SiO<sub>2</sub> wafers and transfer MLG on top of these samples. This is one of the goals of my work at the Low Temperature Laboratory of the University of Salamanca: learn how to exfoliate graphene and h-BN single-crystal for future production of these type of samples.

## **2.1 Hexagonal Boron Nitride**

Hexagonal Boron nitride (h-BN) is a dry lubricant with an hexagonal crystal structure similar to graphite (often called White Graphite). Boron nitride is not found in nature and is therefore produced synthetically. By far, chemical vapor deposition (CVD) has been the most common method to synthesize h-BN over the decades. More difficult is to obtain bulk isolate h-BN single crystals as needed for graphene based electronics, that cannot be obtained by CVD. For this purpose solution/precipitation methods have

been investigated in the last few years obtaining high-quality h-BN crystals with sizes up to 5 mm.

The importance of h-BN is due to different reasons: first of all, h-BN present the same hexagonal crystal structure of graphene and more or less the same lattice constant. A mechanical exfoliated flake presents an atomically smooth surface and it is relatively free of dangling bonds and charge traps: this is due to its insulating nature given by ionic bonds that characterize the crystal lattice. This newly produced material should be used like a gate substrate for graphene, increasing its purity. [3] It is known that graphene on SiO<sub>2</sub> substrate doesn't present the expected quality: carrier mobility is principally limited by surface roughness, scattering with charged surface state and SiO<sub>2</sub> surface optical phonons. The use of exfoliated 20-40 nm-thick h-BN is expected to eliminate these affections and improve graphene-based devices' quality.

Having a look on it, it is an insulating isomorph to graphite, with nitrogen and boron atoms in the A and B sublattices in the Bernal structure (see *Figure 3.*). It presents a 5.97 eV bandgap and a small constant lattice difference with graphene due to the different energies of the two atoms. All these properties motivated the development of this new branch of graphene science, leading to new and successful results.

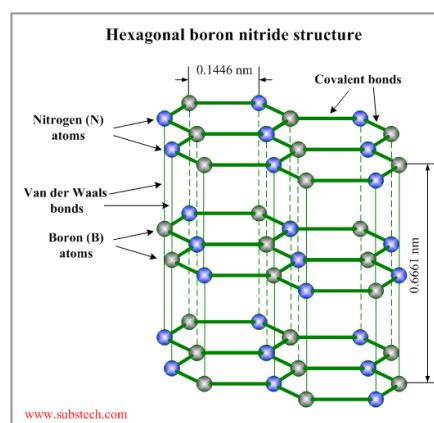


**Figure 3.** Hexagonal Boron Nitride structure. In evidence we can see the A and B atoms of the Bernal stacking.

### 3. Optical characterization

One of the most important properties that Peter Blake, supported by Geim and Novoselov, understood in Manchester was how to detect graphene on the top of a substrate and also how to distinguish the number of layers using just an optical microscope. This is due to the fact that graphene on top of a substrate produces a visible optical contrast: reflected light has different intensity whether you look graphene or only the substrate. The optical contrast depends in particular on the combination of the thickness of the SiO<sub>2</sub> substrate, the light wavelength used to illuminate the sample, the intensity of the light and the thickness of the graphene sample.

The amount of this optical contrast, or vice versa the number of layers (when the contrast is known), should be calculated via the complex Fresnel Equation. [5] We have to consider the light normally incident from air to the sample, taking its refractive index  $n_0 = 1$ , and the sample composed of three different layer of different complex refractive indexes. A representation of the system is painted in *Figure 4.* The one at the backside is thought infinite (for our devices the Si layer) and characterized by a complex refractive index  $n_3(\lambda)$   $\lambda$ -dependent. The second layer is the SiO<sub>2</sub> layer, of thickness  $d_2$  and characterized by a refractive index  $n_2(\lambda)$   $\lambda$ -dependent only real. In this way, considering  $n_3(\lambda)$  and  $n_2(\lambda)$ , it is possible to evaluate and describe the whole of interference colors for the wafer in use. The first layer that the light meets is the graphene sheet: we consider its thickness  $d_1$  equal to the extension of the  $\pi$  orbitals out of plane ( $d_1 = 0.34nm$  for the monolayer, for multi-layer  $d_{1,m} = m \times d_1$ ) and its complex refractive index  $n_1(\lambda) = 2.6 - 1.3i$  independent of  $\lambda$ . Subsequently,

the light meets the SiO<sub>2</sub> and the Si: in particular, for the case of  $\lambda = 400nm$ , the handbooks give us  $n_3(\lambda = 400nm) = 5.6 - 0.4i$  and  $n_2(\lambda = 400nm) = 2.47$  as refractive indexes.

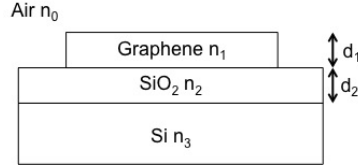


**Figure 4.** Schematic representation of the system considered for the reflected light intensity calculation.

Now, applying the Fresnel law at the system considered above, the reflected light intensity from graphene can be written as:

$$I(n_1) = \left| (r_1 e^{i(\Phi_1 + \Phi_2)} + r_2 e^{-i(\Phi_1 - \Phi_2)} + r_3 e^{-i(\Phi_1 + \Phi_2)} + r_1 r_2 r_3 e^{i(\Phi_1 - \Phi_2)}) \times (e^{i(\Phi_1 + \Phi_2)} + r_1 r_2 e^{-i(\Phi_1 - \Phi_2)} + r_1 r_3 e^{-i(\Phi_1 + \Phi_2)} + r_2 r_3 e^{i(\Phi_1 - \Phi_2)})^{-1} \right|^2 \quad (1)$$

with  $r_1 = \frac{n_0 - n_1}{n_0 + n_1}$ ,  $r_2 = \frac{n_1 - n_2}{n_1 + n_2}$ ,  $r_3 = \frac{n_2 - n_3}{n_2 + n_3}$  the relative indexes of refraction and  $\Phi_1 = \frac{2\pi n_1 d_1}{\lambda}$  and  $\Phi_2 = \frac{2\pi n_2 d_2}{\lambda}$  the phase shifts due to changes in the optical path.

Considering the intensity (1), the contrast  $C$  is defined as the relative intensity of reflected light in presence ( $n_1 \neq 1$ ) or absence ( $n_1 = n_0 = 1$ ) of graphene:

$$C = \frac{I(n_1=1) - I(n_1)}{I(n_1)} \quad (2)$$

In reality, the theory slightly overestimates the contrast: this difference should be attributed to deviation from normal light incidence and to an extinction coefficient of graphene that differs from that of graphite.

Figure 5. is a plot of this contrast function: the color scale gives the intensity of the contrast as a function of SiO<sub>2</sub> thickness  $d_2$  and of the light wavelength  $\lambda$ . This image

should be useful to choose the SiO<sub>2</sub> thickness of the wafer to use: the ones of 90 nm and of 280/300 nm are the substrates that have the highest contrast with white light and green light. They are usually the suggested for graphene's production in common laboratories, where are diffused optical microscopes with white light and color filters. In the Low Temperature Laboratory of Salamanca we have a Leica's optical microscope with white and UV light and a green filter. For graphene production we are accustomed to use 300 nm thick SiO<sub>2</sub> substrates, just sometimes of 90 nm thick.

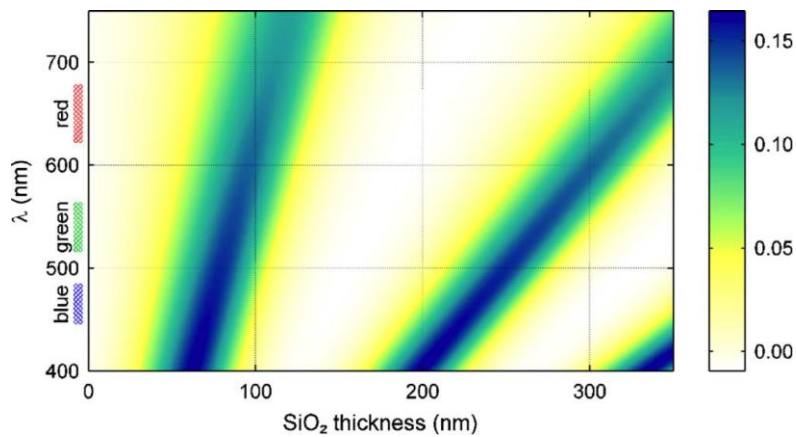


**Figure 5.** Plot of the optical contrast (2) in function of the wavelength and of the SiO<sub>2</sub> thickness. On the right there is the color scale corresponding to the contrast's intensity.

All these calculations and examples are made for mono-layer graphene. If you look at graphene multi-layer (like bi-, tri- and more), the Contrast should increase because of a change of the optical path of  $n_1 \cdot d_1 \rightarrow n_1 \cdot (m \times d_1)$ ; consequently there will be a phase shift  $\phi_1 \rightarrow \phi_1^m = \frac{2\pi n_1(m \times d_1)}{\lambda}$  and the reflected light intensity decrease. *Figure 6.* is an example of comparison between the contrast of mono- and multi-layer graphene sheets.

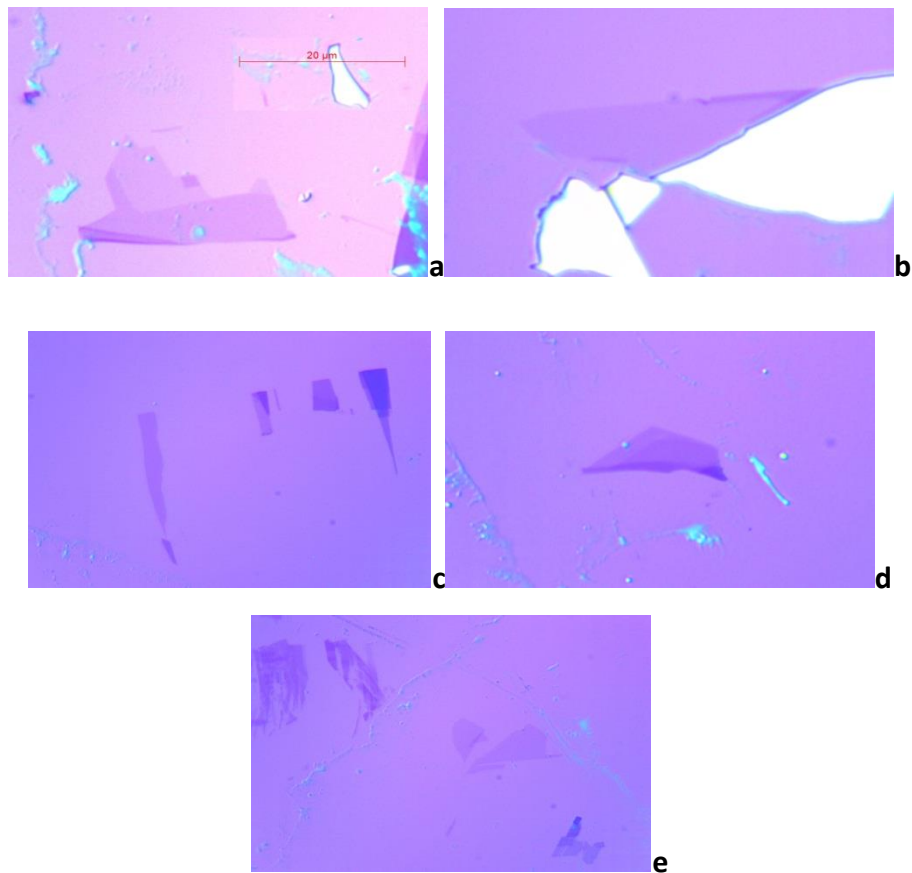


**Figure 6.** Graphene samples: these samples were obtained with the scotch tape technique exfoliating graphite with a 3M scotch tape and transferred on a Si/SiO<sub>2</sub> wafer of 300nm. The contrast is given by the white light LED of the microscope: as should be seen, we can clearly see graphene flakes on this 300nm SiO<sub>2</sub> substrate. a) Graphene mono-layer and bi-layer. b) Graphene mono-layer next to a graphite sheet. c) Graphene nanoribbons; from the left: MLG, MLG, BLG and multi-layer graphene. d) MLG and BLG. e) Mono-layer graphene.

As I told in the introduction, in the same way in which we can produce graphene, we can produce h-BN mono-/multi- layers. At the beginning of my work in Salamanca we used dust of h-BN: since the first times it was clear that from these small pieces (1 – 2 μm) it was possible to take Raman measurements but was impossible to produce large scale layers (tens of μm). After the study of some papers and a long search in the web we found two other possibilities: h-BN single crystal (see in *Figure*

7.), expensive and difficult to find in commerce (we think are grown epitaxially and are at now matter of research) but suitable for exfoliation of large flakes, and crystals, cheaper but “amorphous”. When we bought some of these crystals, we applied the same technique used for MLG production to exfoliate h-BN: using the scotch tape, we mechanically cleaved the h-BN planes and, after the application to a silicon/silicon oxide substrate with a gentle pressure on the scotch, we had to look for the flakes deposited. Again, for this purpose Geim and Novoselov’s Manchester Group had the brilliant idea to apply the same theory for the optical contrast’s calculation used for graphene to the h-BN. [7]

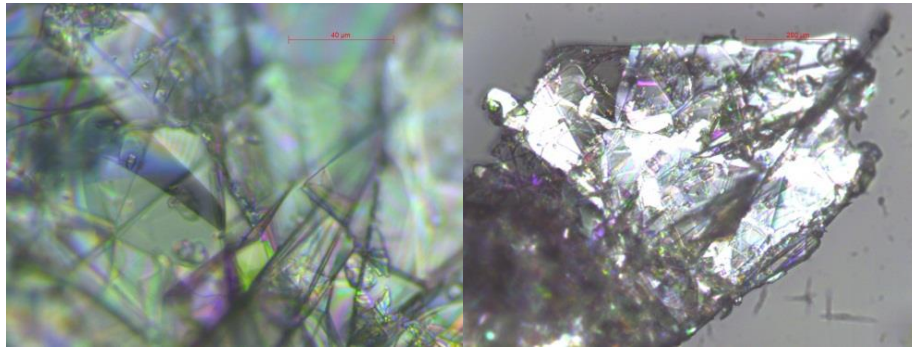


**Figure 7.** h-BN single crystal epitaxially grown. These images were taken with the Leica optical microscope of the LTL of Salamanca: it is the same sample but observed with objectives of different zoom.

From a theoretical and experimental point of view h-BN flakes present a lower contrast to light. The Contrast function should be calculated in a similar way to graphene and based on a matrix formalism of interference in thin film multilayer, substituting  $n_1 = n + ik$  with the one of h-BN obtained with ellipsometric measurements. The theory explained accurately reproduces the observed contrast.

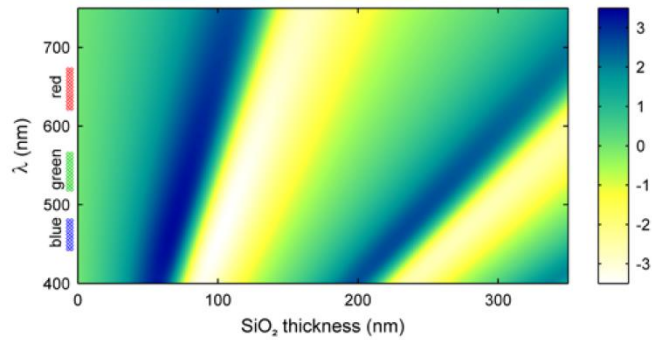


**Figure 8.** Plot of the optical contrast in function of the wavelength and of the SiO<sub>2</sub> thickness. On the right there is the color scale corresponding to the contrast's intensity.

These flakes present a really low contrast even if Si/SiO<sub>2</sub> substrate are used: in particular a monolayer BN on a 300 nm substrates presents a contrast of the order of 1-1.5% using white light. Another typical property of BN is that the optical contrast is not a monotonic function of the light wavelength and changes its sign more or less at  $\lambda \sim 530 \text{ nm}$ : h-BN monolayer is darker than the substrate when at longer wavelength and brighter when at shorter ones. This is totally different from MLG, where we have seen that the contrast is always positive and increases with the number of layers. *Figure 9.* is a plot of the optical contrast for a monolayer and bilayer on a 290 nm SiO<sub>2</sub> wafer, obtained with this theory, which shows the change of sign announced in [7]. Instead *Figure 8.* is a plot, like the one of *Figure 5.* for graphene, of the intensity of the contrast as a function of SiO<sub>2</sub> thickness and of the light wavelength  $\lambda$ . Looking at this graphs it is possible to see that the highest optical contrast is of the order of 2.5-3% for h-BN monolayers on SiO<sub>2</sub> of 80 nm thickness in the entire visible range, but sufficient to hunt h-BN layers.

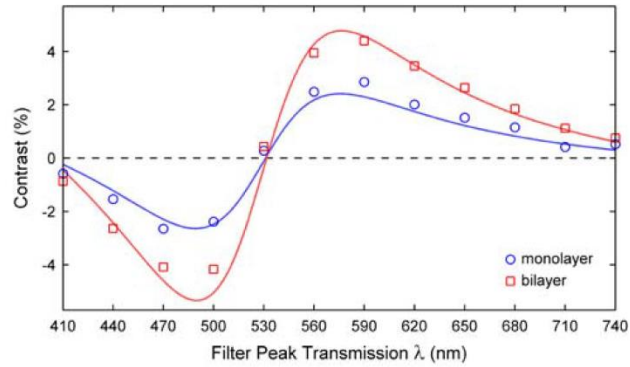


**Figure 9.** h-BN theoretical and experimental optical contrast.

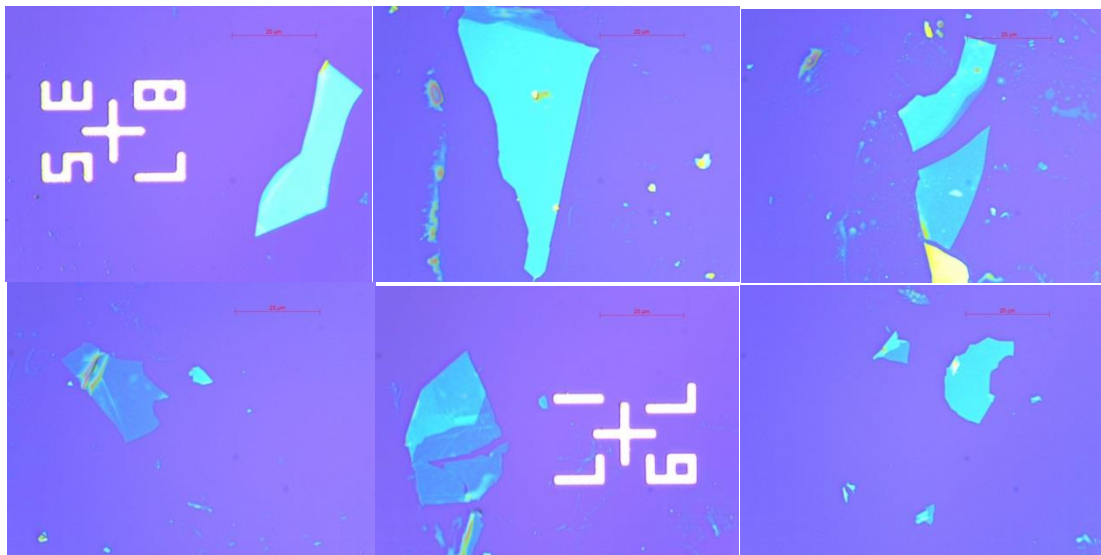


**Figure 10.** Samples of exfoliated h-BN with different number of layers.

For the production of our devices we don't need h-BN monolayers, it's enough to have h-BN layers whose thickness is between 20 nm and 40 nm. This thickness should be attributed from 3 to 10 layer of h-BN; examples are the ones in *Figure 10*. The real importance of the use of this material is principally due to its atomically thick roughness and to its purity as a gate substrate for graphene, as announced in the Introduction.

## 4. Raman spectroscopy

Raman spectroscopy is a spectroscopic technique that allows the study of vibrational, rotational and other low frequency-mode in a system. It was predicted in 1923 by A. Smekal and subsequently discovered by Sir C. Raman in the 30s. It is based on the so-called Raman effect which consists of an inelastic scattering of incident monochromatic photons. Simplifying the theory, monochromatic light from a laser is absorbed by a sample when focused on it. After a relaxation time, light is re-emitted with different frequencies: there are Rayleigh scattering processes (in which photons have the same wavelength and wavevector of the incident light), the Stokes scattering processes (in which the photons have a lower frequency) and the case in which they have an higher frequency (anti-Stokes scattering processes). *Figure 11.* is a scheme of these simplified processes. The intensity of the Rayleigh peak is much more higher than the Stokes and anti-Stokes ones because of a large difference in their scattering probability.

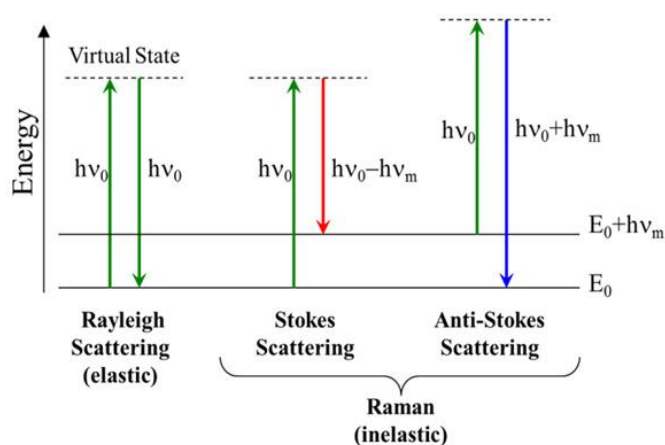


**Figure 11.** Schematic view of the Rayleigh and Raman processes.

Usually laser light used is in the visible, NIR and near-UV: inverting the relation that joints  $\lambda$  and  $q$  it is possible to see that we investigate phonons in the zone centers, because are at small  $q$ . When the laser light is directed to the sample, it interacts with molecular vibrations, phonons and/or other excitations of the system: the photon absorbed polarizes the system and, when the system relaxes, a photon is re-emitted. In the case of a Stokes/Anti-Stokes process, the energy shift gives information on the vibrational characteristics of the material of which the sample is made because it was coupled with them.

Explaining more, in a Raman scattering experiment the energy difference between incident and re-emitted photons is the energy required to excite the molecule to an higher vibrational mode. So photons are absorbed by the molecules, exciting them to a virtual energy state: Rayleigh scattering happens when one molecule relaxes to the initial energy state and the photon emitted has the same frequency value of the incident one. It is also possible that it relaxes in an higher energy state: it means that a phonon has been created. Its energy corresponds to the energy amount needed to excite a vibration in the molecule, which is equal to the difference between initial and final photon frequency. With a lower probability the system relaxes emitting a photon with an higher frequency; this is the case of the Anti-Stokes scattering. The probability is lower because it is needed an excited vibrational state of the molecule to couple with the incident photon. These last two processes have the same displacements  $\Delta\nu$  from the laser frequency. [27]

Summarizing, the frequency shift of the photon is directly related to the energy of the excitation produced in the system as a consequence of the energy conservation's principle:

$$E_{exc} = \pm h(\nu_0 - \nu_1) \quad (3)$$

where the + sign is for Stokes processes and the – sign for the Anti-Stokes processes.

Experimentally, a Raman spectrum is a plot of the intensity of scattered light from a sample as a function of the frequency shift from the incident light. As I told before, usually the intensity  $I$  (in arbitrary units) is reported in function of wavenumbers obtained from this relation:

$$\Delta q = \frac{1}{\lambda_0} - \frac{1}{\lambda_1} \quad (4)$$

From these spectra it is possible to obtain lots of information looking at the position, the number, the intensity and the width of peaks and bands. In particular the Raman spectrum of a material is like its I.D. card thanks to these information. Referring to them, it is possible to identify a given material because each structure has got its own excitations which interact with photons. Moreover Raman spectroscopy is sensible to the quality of the system studied; it can see the presence and the concentration, for example, of defects, impurities and doping.

Similar to this technique is the fluorescence: this process involves the absorption of a photon by the sample. The energy absorbed excites vibrational modes of the material and, when the molecule relaxes, light is re-emitted at different frequencies. So the molecule is brought to an higher or lower energy level. The main difference is that the frequencies of the phonons emitted in a fluorescence process are fixed, depending on the molecule, because are real excited levels. In Raman scattering are involved virtual states; for this reason, the distance of peaks from the excitation one is constant and independent of the wavelength of the absorbed light. So a variation of  $\nu_0$  always implies a variation of  $\nu_1$  because the shift ( $\nu_0 - \nu_1$ ) has to remain constant. Another important difference is the relaxation time of the process. Raman effect is a two-phonon scattering process that takes place in a timescale of the order of  $10^{-15}$  s. Fluorescence instead is a single-photon two-step process and has an relaxation time of the order of  $10^{-9} - 10^{-10}$  s. The third important thing is that the emitted light of a

fluorescence process has a frequency  $\nu_1 < \nu_0$ , so there is not the Anti-Stokes component like in the Raman effect.

As I said before, Raman spectrum is a fingerprint of a material: the interesting parts of the spectra are the Stokes and Anti-Stokes peaks. When this technique is used, people takes the spectra, looks at the characteristics of the peaks (like intensity, FWHM, position, etc.) and compares them to the ones in literature to understand what the material is.

To take these measurements it is used intense, monochromatic, highly collimated, polarized light. A typical Raman setup is composed by:

- a laser source;
- a focusing optic, needed to focalize the laser spot to  $\mu m$  diameter size;
- a collecting optic;
- a notch filter, needed to cut the Rayleigh component of the spectra;
- a monochromator, that selects the range of wavelength refracted to the CCD;
- a light intensity detector, usually a CCD.

The Department of Physics A. Volta of the University of Pavia has got an Hariba Jobin-Yvon spectrometer, used to investigate materials by the Raman effect. In particular, this instrument has a 632 nm He-Ne laser and some objective that can focus the laser spots until  $1\mu m^2$  of area. Light is collected in backscattering configuration.

## 4.1 Raman spectrum of graphene

As I told before, production of graphene mono-layer is not so easy. When someone finds a flake of graphene needs to know its characteristic, like the number of layers and the quality. In particular, the use of optical contrast to distinguish between the number of layers leads to ambiguous results because the contrast depends on the type and on the thickness of the substrate. AFM is usually used in this type of measurements because of its precision but it is a technique with low throughput. Another developed technique applied in this field is the Raman spectroscopy. Thanks to this method, we can capture uniquely graphene's electronic structure. Spectra measured reflect the changes in the electronic bands of MLG, BLG and multilayer, leading to a nondestructive and unambiguous understanding of the graphene sample. Furthermore, Raman spectra can provide information about doping, defects and information on edges of graphene flakes.

Going through the Raman theory well known of all carbon systems, it is possible to note that the spectrum of these materials shows only a few prominent features and appears really simple: just a couple of intense bands in the  $1000\text{-}2000\text{ cm}^{-1}$  region and a few of other second-order modulations. The main features in these spectra are the so-called G, D and 2D peaks, which are more or less at  $1580\text{ cm}^{-1}$ , at  $1360\text{ cm}^{-1}$  and at  $2650\text{ cm}^{-1}$ ; they are principally due to resonances with the  $\pi$  states, so the spectra is dominated by  $sp^2$  sites. The G peak is usually attributed to the bond stretching of all pairs of  $sp^2$  atoms in both rings and chains. The D one is due to the breathing modes of  $sp^2$  atoms in rings. [4]

The D peak for graphene is attributed to an  $A_{1g}$  breathing mode at  $\mathbf{K}$ , activated by a double resonance (DR) process. In this picture, Raman scattering is a fourth order

process described by these passages: (i) a laser induces excitation of an electron/hole pair; (ii) electron-phonon scattering with an exchanged momentum  $q \approx K$ ; (iii) defect scattering; (iv) electron/hole recombination. The DR condition is reached when all of these conserve the energy. If we consider graphene, it has four phonon branches at around  $K$  but only one has significant intensity. The others should be Raman active without considering the Electron Phonons Couplings (EPC). Summarizing, the D peak is due to LO phonons around  $K$ , is activated by double resonance and is strongly dispersive with excitation energy due to the Kohn anomaly at  $K$ . So this peak is present only in disordered graphene or in presence of defects: if we have a look in bulk and pure graphene it shouldn't be present. Interesting is that it is always present in spectra taken at the sample edge. An example of this could be seen in *Figure 12.*, which are spectra of bulk graphite.

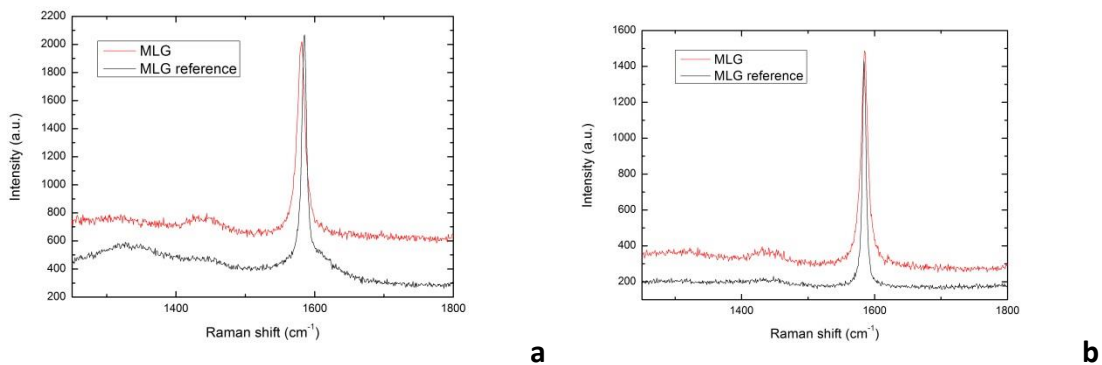


**Figure 12 a-b.** Experimental Raman G and D peak of mono-layer graphene. In the plot we can also see a mono-layer certified sample's spectra, used like a reference for our measurements.

A similar process should happen intra-valley of the phonon spectra, resulting in another peak called D' at around  $1620 \text{ cm}^{-1}$  due to activated phonons at small  $q$ .

Another important feature in C-based materials spectra is the 2D band. It is named in this way because is the second order of the D peak. In MLG appear a single and sharp 2D peak, as can be seen in *Figure 13.*, due to two phonons with opposite momentum

in the highest optical branch near the **K** point in the BZ. It is demonstrated that this peak changes its position while excitation energy changes, at twice the rate of D peak, due to the DR process. Bilayer graphene has a much broader and upshifted 2D band: it has four components,  $2D_{1B}$ ,  $2D_{1A}$ ,  $2D_{2A}$ ,  $2D_{2B}$ , two of which ( $2D_{1A}$  and  $2D_{2A}$ ) have higher relative intensities than the others. The presence of these four components is principally due to the splitting of the electronic bands: the interaction of graphene planes causes the  $\pi$  and  $\pi^*$  bands division in four bands, with a different splitting for electrons and holes. So, without discussing all the theory at the base of the process, result four processes that involve phonons with momenta  $q_{1B}$ ,  $q_{1A}$ ,  $q_{2A}$  and  $q_{2B}$  (due to strong dispersion of the phonon bands around **K**). However,  $q_{1A}$  and  $q_{2A}$  are associated to processes more intense than the other two. Treating the case of graphite, this band is instead characterized only by two components:  $D_1$  and  $D_2$ .

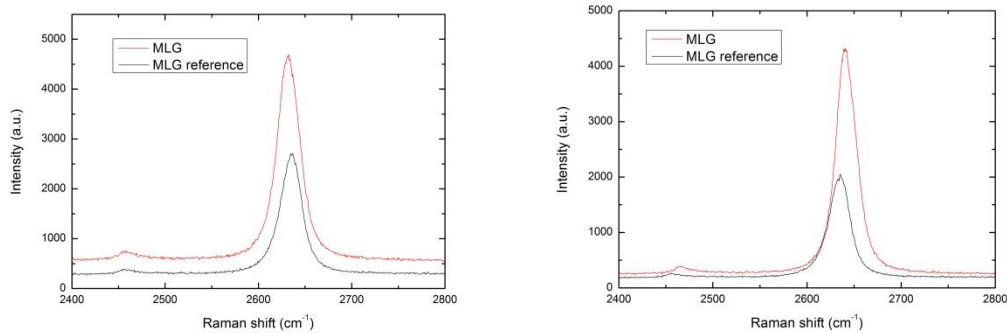


**Figure 13.** MLG's Raman 2D peak.

While looking MLG Raman spectra, one of the most intense peaks is the G peak (see *Figure 12*. again). It is usually attributed to the bond stretching of all pairs of  $sp^2$  atoms in both rings and chains and it is really important because of its sensibility to doping. This happens because doping changes the Fermi surface of graphene and so moves the Kohn anomaly away from  $\mathbf{q} = \mathbf{0}$ . In particular the G peak upshift its position for both holes and electrons; this should be understood using the Density Functional Theory

(DFT). Another important characteristic of this peak is its FWHM: it decreases with temperature and increases with the increase of doping. The third important parameter of G peak is the intensity: the ratio  $I(2D)/I(G)$  also is an index of doping, decreasing while increasing doping level.

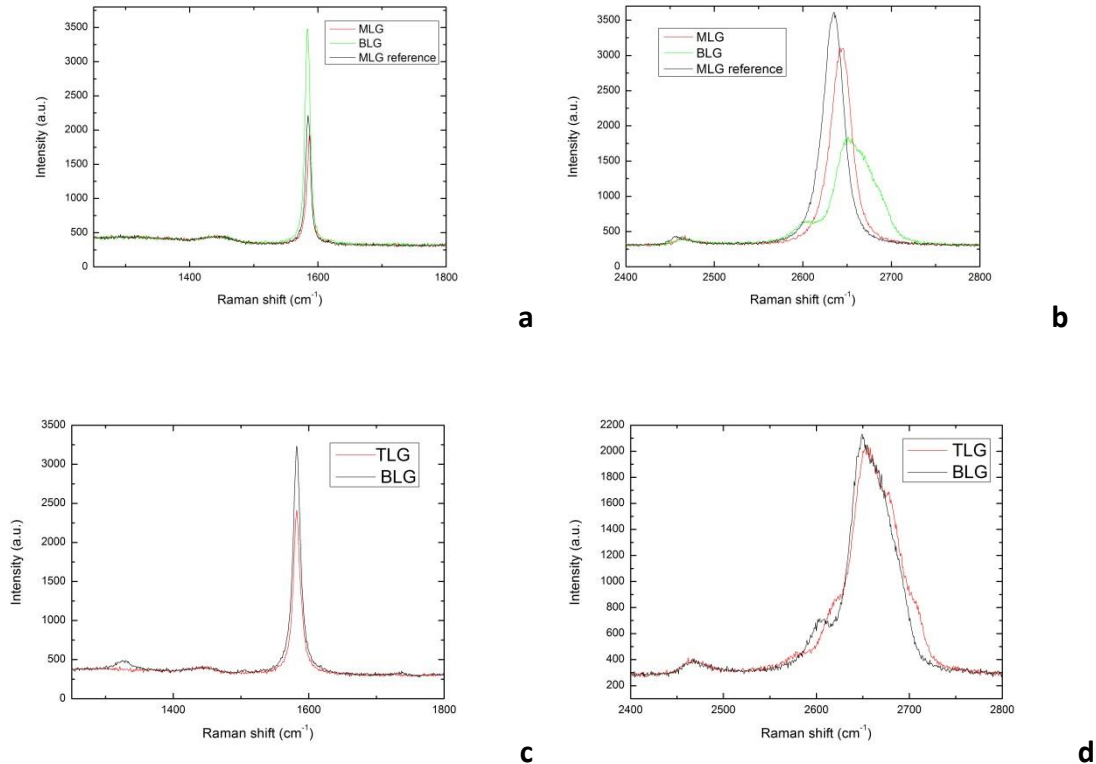


**Figure 14 a-b-c-d.** In graph **a** and **b** there's a comparison between G, D and 2D peak of MLG and BLG. In figure **c** and **d** is plotted the superposition of a bi- and a tri-layer graphene spectra.

Looking at all these features it is possible to characterize a graphene flake until 5 layers. As can be noted in *Figure 14.*, we compare the spectra of MLG, BLG and TLG to understand the difference on the peaks cited before.

It is also possible to understand the doping level of one layer. We used this technique to study the samples produced in the Low Temperature Laboratory of Salamanca, thanks to the Hariba Jobin-Ivon Raman instrument of the University of Pavia.

## 4.2 Raman spectrum of h-BN

Raman spectroscopy is also an useful tool for research on boron nitride. As known, BN has two crystal structures: cubic and hexagonal. For the Raman intensity point of view, h-BN Raman efficiency is two to three orders of magnitude larger than in the cubic one: this means that this technique is capable to measure the presence ratio between the two phases in a sample (h-BN purity).

In particular, h-BN exhibits a characteristic peak that is due to the  $E_{2g}$  phonon mode and analogous to the G peak of graphene. The boron and the nitrogen atoms in each plane move in opposite directions and the atomic displacements in the two planes are combined symmetrically. Interestingly, this mode does not have an LO-TO splitting, since the contributions from the two planes cancel each other. This is the Raman-active high-energy phonon at  $1366\text{cm}^{-1}$ . In its spectrum there is another peak, smaller than the other, at  $55\text{cm}^{-1}$ . [8]

As it was noted by Geim, Novoselov and Blake in [7], the peak at  $1366\text{cm}^{-1}$  becomes progressively weaker as N (number of layers) decreases. For h-BN monolayer, its intensity is 50 times smaller than in graphene G peak and the integrated intensity is proportional to N with high accuracy. In addition, this Raman peak in monolayer BN is usually upshifted and in bilayer h-BN is downshifted with respect to bulk h-BN. To explain these variations, the Group of Manchester invoked strain that causes additional sample-dependent red shifts in the case of stretching. This behavior is not present in graphene because of the larger presence of doping effects. Considering h-BN, it is free of doping for its insulating character and strain is important to determine the Raman peak position.

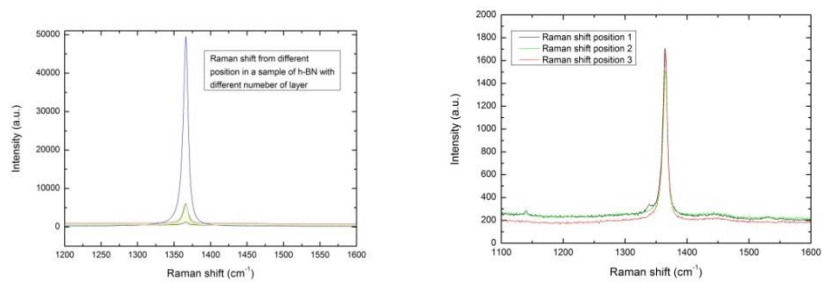


**Figure 15.** In the left graph it is plotted a superposition of Raman spectra of h-BN samples with a different number of layers. On the right instead there's a superposition (quasi-perfect) of spectra of the same h-BN sample at different position.

Following their studies, in Pavia we measured Raman spectra from samples with h-BN flaxes transferred onto Si/SiO<sub>2</sub> wafers. We compare our samples with one produced by Peter Blake in Graphene Industries (Manchester, UK). The characteristics announced were confirmed in these samples as we should see in *Figure 15.-left*, which is a superposition of Raman spectra of sample with different number of layers. On the other hand we also prepare several samples exfoliating at the same time h-BN and graphite obtaining superposition of multilayer h-BN and graphene onto Si/SiO<sub>2</sub> wafers. Their Raman spectra are shown in *Figure 16.*

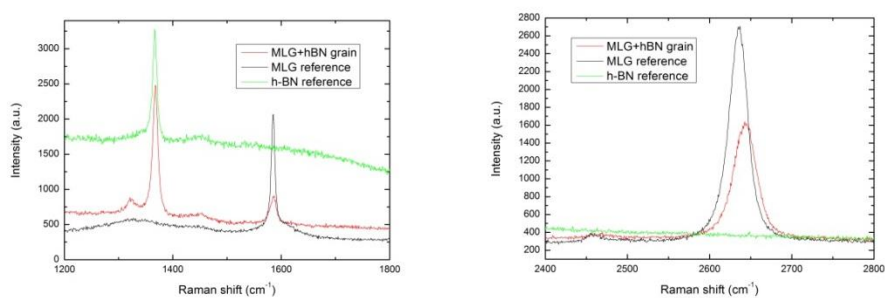


**Figure 16.** Spectra of G and 2D peaks of graphene superposed with h-BN spectra. It is clear the presence of the h-BN peak at  $\sim 1366\text{cm}^{-1}$ . Interesting is the plot in red: this is the spectrum of an h-BN grain between SiO<sub>2</sub> and a MLG sample. As it can be seen, the system has a total spectrum with both the characteristics of the materials.

## 5. Electronic properties of graphene

Graphene's energy bands were studied since 1946, firstly by P. R. Wallace who evidenced its semi-metallic behavior.

Graphene is made out of carbon atoms organized in an hexagonal crystalline structure (see *Figure 17.*): this is not a Bravais lattice and can be decomposed in a triangular lattice with a basis of two atoms per unit cell. By this approximation it is possible to write the lattice vectors in the following way:

$$a_1 = \frac{a}{2}(3, \sqrt{3}) \qquad a_2 = \frac{a}{2}(3, -\sqrt{3}) \qquad (5)$$

with  $a \approx 1.42 \text{ \AA}$  carbon-carbon distance. Instead the reciprocal lattice vectors can be written in this way:

$$b_1 = \frac{2\pi}{3a}(1, \sqrt{3}) \qquad b_2 = \frac{2\pi}{3a}(1, -\sqrt{3}) \qquad (6).$$

In energy band structure physics, really important are the  $\mathbf{K}$  and  $\mathbf{K}'$  points of the Brillouin Zone (BZ). They are named *Dirac points* and their positions in momentum space are given by:

$$\mathbf{K} = \left(\frac{2\pi}{3a}, \frac{2\pi}{3\sqrt{3}a}\right) \qquad \mathbf{K}' = \left(\frac{2\pi}{3a}, -\frac{2\pi}{3\sqrt{3}a}\right) \qquad (7).$$

In real space the nearest neighbors vectors are written:

$$\delta_1 = \frac{a}{2}(1, \sqrt{3}) \qquad \delta_2 = \frac{a}{2}(1, -\sqrt{3}) \qquad \delta_3 = -a(0,1) \qquad (8).$$

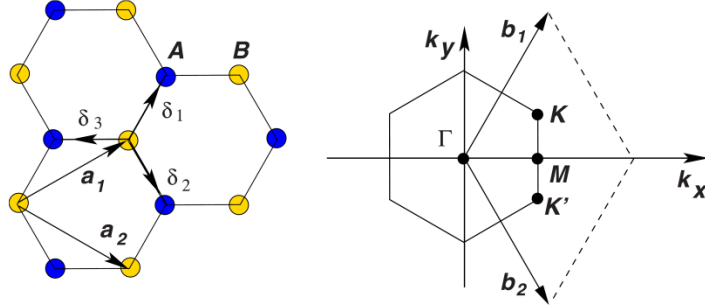


**Figure 17.** Left: lattice structure of graphene, made out of two interpenetrating triangular lattices. Right: corresponding Brillouin zone; the Dirac cones are located at the  $K$  and  $K'$  points.

The starting point for the energy band calculation is the Tight-binding Hamiltonian for the electrons in graphene; it is important to consider both the hopping of electrons with the nearest neighbors and with the second- (or next-)nearest neighbors. So the Hamiltonian, in units of  $\hbar = 1$ , take the form:

$$H = -t \sum_{\langle i,j \rangle, \sigma} (a_{\sigma,i}^+ b_{\sigma,j} + h.c.) - t' \sum_{\langle\langle i,j \rangle\rangle, \sigma} (a_{\sigma,i}^+ a_{\sigma,j} + b_{\sigma,i}^+ b_{\sigma,j} + h.c.) \quad (9)$$

where  $a_{\sigma,i}^+$  ( $a_{\sigma,i}$ ) is the operator that annihilates (create) an electron with spin  $\sigma$  in the site  $\mathbf{R}_i$  on sublattice A (equivalently for  $b_{\sigma,i}^+$  and  $b_{\sigma,i}$  in the site B);  $t$  is the nearest neighbors hopping energy ( $t \approx 2.8eV$ );  $t'$  is the next nearest neighbors hopping energy. Graphene's energy bands are derived from the Hamiltonian (9), diagonalizing it with the basis given by the eight Bloch's sum of type:

$$\Phi_v^i = \frac{1}{\sqrt{N}} \sum_{\mathbf{t}_m} e^{i\mathbf{k} \cdot \mathbf{t}_m} \phi^i(\mathbf{r} - \mathbf{d}_v - \mathbf{t}_m) \quad (10)$$

( $i=2s, 2p_x, 2p_y, 2p_z$ ;  $\mathbf{t}_m$  generic translational vector;  $\mathbf{k}$ : Bloch vector of the reciprocal space;  $N$ : number of unit cells). These bands have the form:

$$E_{\pm}(\mathbf{k}) = \pm t \sqrt{3 + f(\mathbf{k})} - t' f(\mathbf{k}) \quad (11)$$

with

$$f(\mathbf{k}) = 2 \cos \sqrt{3}k_y a + 4 \cos \frac{\sqrt{3}}{2}k_y a \cos \frac{3}{2}k_x a \quad (12)$$

where + is for the upper  $\pi$  band and – is for the lower  $\pi^*$  band: these two are the upper valence and lower conduction bands and are due to the out of plane interaction between the  $2p_z$  orbitals. In this solution there is bands' symmetry around zero energy only when  $t' = 0$ ; when this condition is not satisfied (and  $t'$  has a finite value) bands become asymmetric.

The band structure of graphene is painted in *Figure 18.*; in the same picture it is zoomed the band structure close to the Dirac points ( $\mathbf{K}$  and  $\mathbf{K}'$  in the BZ). From equation (11) and (12) it is possible to obtain this energy dispersion relation expanding in series  $f(\mathbf{k})$  near the  $\mathbf{K}$  and  $\mathbf{K}'$  points and substituting  $\mathbf{k} = \mathbf{K} + \mathbf{q}$ , with  $|\mathbf{q}| \ll |\mathbf{K}|$  (13):

$$E_{\pm}(\mathbf{q}) \approx \pm v_F |\mathbf{q}| + \mathcal{O}((q/K)^2) \quad (14)$$

where  $\mathbf{q}$  is the momentum measured respect to the Dirac point and  $v_F = 3ta/2 \approx c/300 \approx 10^6 \text{ m/s}$  the Fermi velocity. Most of the unique properties of electrons in graphene derive from this unusual linear dispersion relation. This result is really important because it is different from any other band structure of semiconductor (which usually has the form  $(\mathbf{q}) = \hbar^2 q^2 / 2m$ ) and the Fermi velocity does not depend on the energy or momentum.

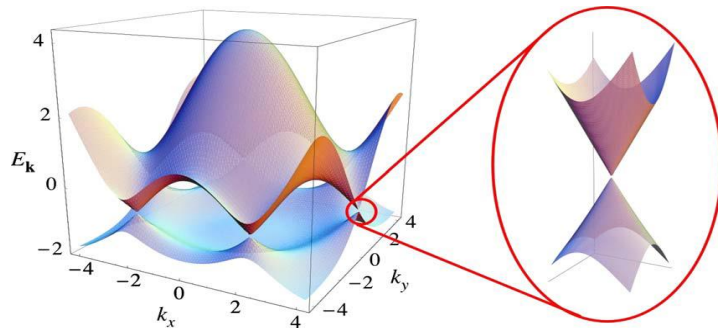


**Figure 18.** Energy spectrum (in units of  $t$ ) for finite values of  $t$  and  $t'$ , with  $t = 2.7eV$  and  $t' = -0.2t$ . On the right are zoomed the energy bands close to one of the Dirac points.

When the condition for the expansion (13) is not satisfied, it is needed to consider other terms of the expansion and to consider the  $t'$  term of the Hamiltonian. The  $t'$  term shifts in energy the position of the Dirac point and breaks the electron-hole symmetry, while the other terms of the expansion give the so-called trigonal warping of the electronic spectrum, characterized by a three-fold symmetry.

Starting again from Eq. (9), deriving the theory close to the Dirac points and expanding in Fourier series the electron operators, the effective Hamiltonian presents two copies of the massless Dirac-like Hamiltonian. In particular the two components electron wavefunction  $\psi(\mathbf{r})$  close to the  $\mathbf{K}$  point obeys to the 2D Dirac equation

$$-iv_F \boldsymbol{\sigma} \cdot \nabla \psi(\mathbf{r}) = E \psi(\mathbf{r}). \quad (15)$$

The wavefunction in the momentum space, around  $\mathbf{K}$ , has the form:

$$\psi_{\pm, \mathbf{K}}(\mathbf{k}) = \frac{1}{\sqrt{2}} \begin{pmatrix} e^{-i\vartheta_k/2} \\ \pm e^{i\vartheta_k/2} \end{pmatrix} \quad \text{for} \quad H_{\mathbf{K}} = v_F \boldsymbol{\sigma} \cdot \mathbf{k} \quad \text{and} \quad \vartheta_k = \arctan \frac{q_x}{q_y} \quad (16)$$

while around  $\mathbf{K}'$ :

$$\psi_{\pm, \mathbf{K}'}(\mathbf{k}) = \frac{1}{\sqrt{2}} \begin{pmatrix} e^{i\vartheta_k/2} \\ \pm e^{-i\vartheta_k/2} \end{pmatrix} \quad \text{for} \quad H_{\mathbf{K}'} = v_F \boldsymbol{\sigma}^* \cdot \mathbf{k} \quad (17)$$

with  $\mathbf{k}$ : momentum operator and  $\boldsymbol{\sigma} = (\sigma_x, \sigma_y)$  that is the *pseudospin* ( $\sigma_x$  and  $\sigma_y$  are the Pauli's matrixes).

These two wavefunction are related by the time reversal symmetry: fixing the origin of coordinates in momentum space in the M-point of the BZ, time reversal is the same of a reflection along  $\mathbf{k}_x$  axis. Wavefunctions (16) and (17) are spinors; one of most interesting spinor's property is the rotation: if the phase  $\vartheta$  is rotated by  $2\pi$ , the wavefunction changes sign indicating an additional phase of  $\pi$  (commonly called Berry phase).

Another important quantity to consider is the helicity, used to characterize the eigenfunction. This operator is defined as the projection of the momentum operator along the pseudo-spin direction and has the form:

$$\hat{h} = \frac{1}{2} \boldsymbol{\sigma} \cdot \frac{\mathbf{p}}{|\mathbf{p}|} \quad (18)$$

for which the states  $\psi_{\mathbf{K}}(\mathbf{r})$  and  $\psi_{\mathbf{K}'}(\mathbf{r})$  are eigenstates:

$$\hat{h}\psi_{\mathbf{K}}(\mathbf{r}) = \pm \frac{1}{2} \psi_{\mathbf{K}}(\mathbf{r}) \quad (19).$$

Therefore electrons (holes) have a positive (negative) helicity. Equations (19) says also that  $\boldsymbol{\sigma}$  has its two eigenvalues in the direction parallel or antiparallel to the momentum  $\mathbf{p}$ . This means that the states of the system close to the Dirac point have well defined chirality or helicity. Helicity values are good quantum numbers as long as Hamiltonian re-written to obtain Eq. (15), and its approximation, are valid. The chiral nature of the charge carriers implies that they can perform Klein tunneling, i.e. at normal incidence  $T = 1$  through any potential barrier.

## 5.1 Dirac peak

An important feature in graphene is the Dirac peak. Electrons and holes exhibit QED's charge-conjugation symmetry thanks to the properties we have explained before. This symmetry can be experimentally demonstrated by performing electric field effect's measurements: one can continuously tune the Fermi level by applying a back-gate potential (in our devices to the SiO<sub>2</sub>) to evaluate all the double cone structure. In fact

graphene exhibits an ambipolar conductivity: the same transport properties are given by electrons and holes, respectively at  $V_g > 0$  and  $V_g < 0$ . At  $V_g = 0$  the Fermi level is at the degeneration point: no charge carrier should be excited, so it is expected an infinite resistivity. This point is called Charge Neutrality Point (CNP). In *Figure 19*. We show a simulation of the Dirac peak in graphene with painted its energy bands and the position of the Fermi level for the three cases explained.

In reality happens that near the CNP resistivity value is finite; this means that there's a finite number of charge carriers and near the CNP holes and electrons' regime is mixed: the current is provided both from positive and negative carriers simultaneously. This effect is principally due to irregularities and corrugations which affects real graphene samples: in this picture, irregularities and corrugations make the gate potential applied non-uniformly across the whole sample, thus producing the so-called electron-hole puddles.

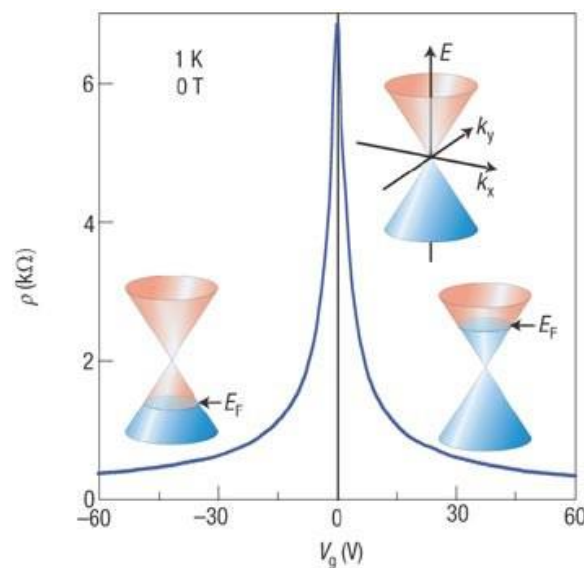


**Figure 19.** Electric field effect in graphene.

## 5.2 Hall effect

The quantum Hall effect (QHE) does not depend on the sample properties but it is a universal property of 2D systems. In particular requires a system containing a 2DEG and the presence of disorder.

The QHE appears as the quantization of the transverse resistivity into well-defined plateaus with the series:  $\rho_{xy} = \frac{h}{ne^2} (20)$ , with  $h$  Planck's constant and  $e$  the electronic charge.

Prof. Klaus Von Klitzig discovered the Integer QHE (IQHE) where  $n$  has an integer positive value; a few years later the group of Prof. Daniel Tsui discovered the Fractional QHE (FQHE), where  $n$  is a fractional number. The origin of the two phenomena is really different: the explanation of the FQHE needs the use of Quantum Field Theory and this goes beyond the aim of this thesis. The plateaus' values are really accurate, independently on the sample. [22]

An interesting thing is that, when measuring at the same time Hall and longitudinal resistances ( $\rho_{xx}$  and  $\rho_{xy}$ ), while  $\rho_{xy}$  presents a plateau,  $\rho_{xx}$  vanishes to zero and while  $\rho_{xy}$  transits from a plateau to another,  $\rho_{xx}$  presents a peak called Shubnikov de-Haas peak (SdH peak). An example is plotted in *Figure 20*.

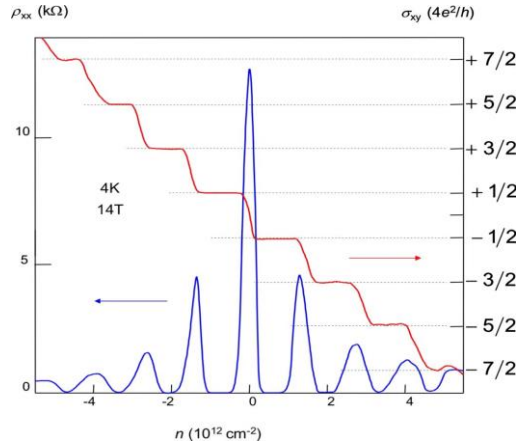


**Figure 20.** Longitudinal resistivity (blue) and Hall conductivity (red) plotted as a function of charge carrier density. It shows the anomalous QH sequence due to the zero energy Landau Level.

Graphene is the unique real 2D system known and presents the QHE. The conventional integer quantum Hall quantization of the conductivity (and of the resistivity) is shifted by  $1/2$  (for this is called semi-integer) because the state at the Landau Level  $n = 0$  is half-filled in comparison with the other levels:

$$\sigma_{xy} = \frac{4e^2}{h} \left( n + \frac{1}{2} \right) = \frac{\nu e^2}{h}, \quad (21)$$

where 4 accounts for the double spin and valley degeneracy,  $n$  is an integer number and  $\nu$  the filling factor. Then the expected sequence of the plateau for the IQHE should be  $= \pm 2, \pm 6, \pm 10, \dots$ . The Equation (21) directly comes from the QED-like quantization of electronic levels in non-zero magnetic field (Landau Levels), which reads

$$E_N = \pm v_F \sqrt{2e\hbar B N} \quad (22)$$

where sign + refers to electrons and – to holes. This last relation implies the presence of a zero-energy level equally shared by electrons and holes, which gives rise to the anomalous sequence. This should also be seen as a manifestation of the semi-period shift induced by the  $\pi$  Berry phase.

## 6. Magnetotransport experiments

Magnetotransport measurements were made at the Low Temperature Laboratory of the University of Salamanca, Spain. This laboratory is equipped with a lot of useful facilities, like 4 lock-ins, two cryostats and a 12 T magnet. For our purposes, we employed the He<sub>3</sub> cryostat HelioxAC-V Salamanca produced by Oxford Instruments: it is a Cryofree system and the helium 3 is re-utilized by the equipment thanks to a system of pumps and traps. When the sample is setted in the cryostat and cooled at  $T \sim 3 \div 5 K$ , it is simply re-cooled down to  $T \sim 250 \div 300 mK$  thanks to the way it is projected (see *Figure 21.*) and stays at this temperature for more or less 50 hours. To re-cool the sample, the process is simple and takes a couple of hours: firstly the Switch Heater has to be switched off; secondly, when  $T_{SH} < 5K$ , the Sorb (adsorption pump) has to be heated till  $T_{Sorb} = 50K$ . In this way all the <sup>3</sup>He in the Sorb is re-liquefied and, after the switching off of the Sorb, the Heater switch heated at  $T_{SH} = 35K$  gives the possibility to the system to reach again  $T \sim 250 - 300 mK$ , because it pumps <sup>3</sup>He gas from the pot to the Sorb (that trapped it until the re-cooling). The temperature of this system is really stable and permits to obtain good transport and magneto-transport measurement thanks to the four lock-in system and to the 12 T magnet.

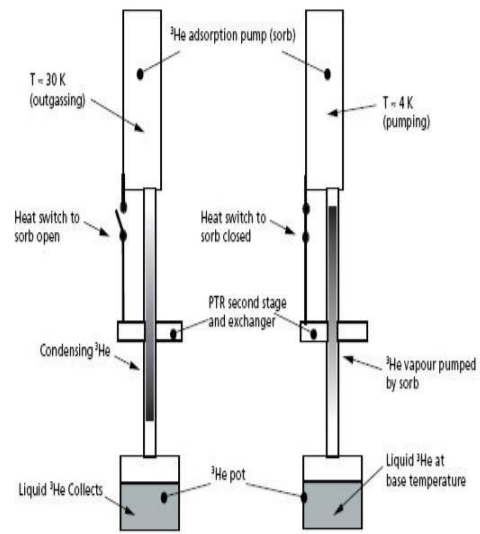


Figure 2: Working principle of the HelioxAC-V\*

**Figure 21.** Picture of the system used to reach 300mK and 12T (left). It is the so-called HelioxAC-V of the LLT of Salamanca. On the right there's painted the working principle of the cryostat that permits to lower the temperature.

## 6.1 Experimental results

At the Low Temperature Laboratory we concentrate our work on a sample of mono-layer graphene transferred over an h-BN flake deposited on a highly doped Si wafer with a 500 nm SiO<sub>2</sub> layer. Au/Ti contacts were defined by means of e-beam nanolithography. The sample production is something pioneering and, as usually happens in electronics, the efficiency of devices working is really low. To produce a sample like this, first of all we have to mechanically exfoliate both h-BN on SiO<sub>2</sub> and graphene on PMMA; secondly we have to superimpose graphene on h-BN implying a micro-manipulator and we have to apply a chemical procedure to remove polymer's

residuals. As a last thing, we have to contact the sample in a Hall bar configuration (Au/Ti contacts deposition). In each of these steps there should be something that affects the possibility of good working of the sample: there should be material between graphene and h-BN, contacts that are not aligned, contacts that doesn't work properly and inhomogeneity of the sample itself. All these problems should be seen when we perform transport and magneto-transport measurements.

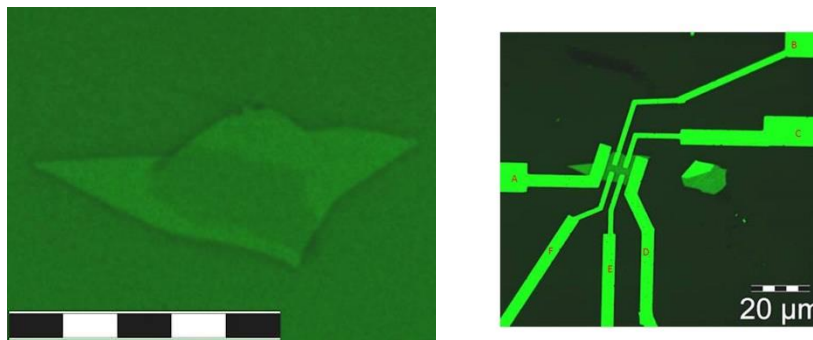


**Figure 22.** Images of the sample BNSD1S3HB2 before (left) and after (right) the deposition of the contacts. In the one on the left it is possible to see the MLG flake on the h-BN substrate thanks to their optical contrasts.

Thanks to the equipment, it is possible to perform two principal types of measurements at fixed temperature. The first one is, while injecting current ( $I = 10 \text{ nA}$ ) between two contacts, to measure the potential difference between contacts parallel to the flux of current while varying the gate potential for a fixed magnetic field: in this way we obtain the so-called Dirac peak. These are called transport measurements. The other type that we can perform is called magneto-transport measurement. Fixed a gate potential (positive or negative), we measure longitudinal and Hall potential difference between different couples of contacts: elaborating data (considering the current injected and the geometry of the sample), longitudinal and Hall resistivities are simply obtained.

In our experiments we made both type of measurements varying contacts configurations. In particular at  $T \sim 300\text{mK}$  we performed measurements varying  $V_{\text{Gate}}$  between  $-15\text{V} < V_{\text{Gate}} < 15\text{V}$  and the magnetic field between  $-9\text{T} < B < 9\text{T}$ . The sample used (named BNSD1S3HB2, *Figure 22.*) is a MLG on h-BN on a substrate of Si with a 500nm  $\text{SiO}_2$  top layer in a Hall bar configuration of  $W \times L = (5.4 \times 9.2)\mu\text{m}$ ; it presents 50-500 Å-thick 6 contacts of Ti/Au deposited with e-beam nanolithography. For our purposes we injected a current of 10nA from the Source to the Drain contacts using a generator of AC voltage (5V at 13Hz) and a resistance of 500M $\Omega$ . As a preliminary step, we produced at  $T \sim 310\text{K}$  and  $B = 0\text{T}$  measurements of longitudinal resistance  $R_{xx}$  as a function of  $V_g$  obtaining a first plot of the Dirac peak. Subsequently we performed the same measurement at  $T \sim 300\text{mK}$ , at  $T \sim 77\text{K}$  and at  $T \sim 233\text{K}$ : we report these graphs in *Figure 23.* and *Figure 24.*

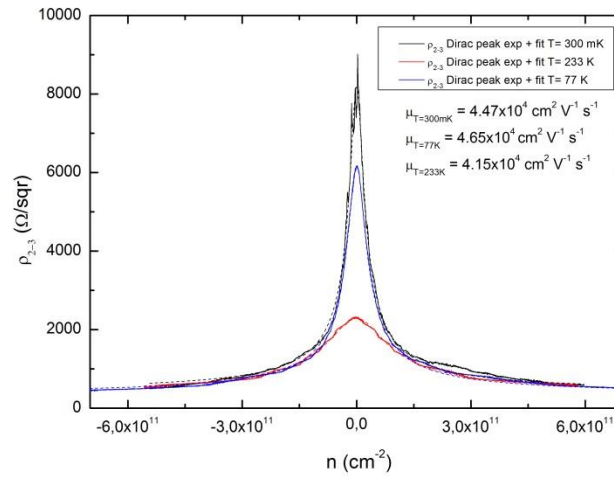


**Figure 23.** Dirac peak at three temperatures, 233K, 77K and 300mK. With the same color are superimposed the fits we made to obtain the mobility, reported in the same graph.

One of our first interests was to fit the Dirac peak of the sample (*Figure 24.*). To do this we followed the standard procedure described in [17]. Considering the Dirac peak at

$T \sim 300 \text{ mK}$ , with this procedure we estimated the position of the CNP and the presence of residual charge density  $n_{res} \cong 1.72 \cdot 10^{10} \text{ cm}^{-2}$ , whom suggests the presence of doping impurities in the sample. We obtained this value using the empirical relation  $n_{res} \cong 0.2 \times n_{imp}$ , which gives us a value of impurities' concentration of  $n_{imp} \sim 8.6 \cdot 10^{10} \text{ cm}^{-2}$ .

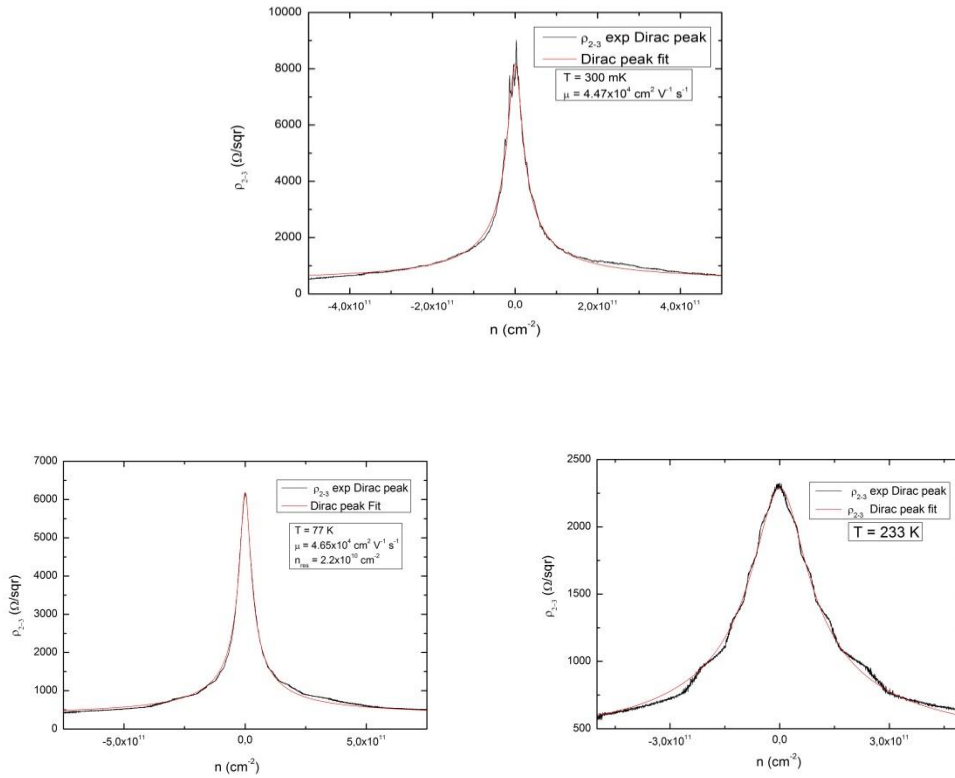


**Figure 24.** The three images are Dirac peaks of the sample at different temperatures. As it can be seen, there are reported the temperature, the mobility and the density for the ones at 300mK and 77K. The are also plotted in red the fit functions of each experimental peak (black).

Subsequently we proceed performing magneto-transport measurements of the Hall resistance  $R_{xy}(B)$  varying  $-9T < B < 9T$  at  $V_{gate} = 0; \pm 2V; \pm 4V; \pm 6V; \pm 8V; \pm 10V; \pm 15V$ , again at  $T \sim 300 \text{ mK}$ , in order to evaluate both the bidimensional charge carriers' density  $n$  and the mobility  $\mu$ . For this

purpose we made use of the standard formulas  $n = \frac{1}{es}$ , where  $s = \frac{dR_{xy}}{dB}$  is the slope obtained with the linear fit of the  $R_{xy}$  vs  $B$  plot in Figure 25..

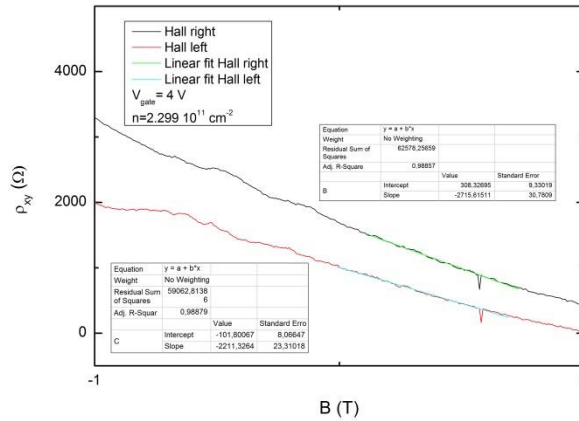


**Figure 25.** Linear fit of the  $R_{xy}$  vs  $B$  for both the left and right Halls. The slope obtained is fundamental for the calculation of the charge carrier density  $n$ .

We applied the same procedure for each  $V_g$  (Figure 26.): results are plotted in Figure 27., which presents also the linear fits of density, and in Tab. 1, where are presented the density of carriers, its error and the mobility for each case. For the calculus of the error we consider the error due to the sensibility of the instruments, the electronic noise and the error in the selection of the interval for the fit. The first one (sensibility) is small respect to all the other sources of error. Successively we consider the second type: we performed measurements without  $B$  field and without  $V_g$  variations to obtain an average value of the electronic noise but the error obtained was too small respect to the third one. To calculate the last type of error, we repeated the fit 4 times for each  $V_g$  taking different intervals; we took the error on the slope given by the linear fit and we used the error propagation theory to calculate the density's error. The total error attributed to each value is, finally, the square root of the sum in quadrature of each one of the 4 errors calculated before. The value is more or less the same for each

$V_g$  and is one order of magnitude less than the density ( $\delta n \sim 6 \cdot 10^9 \text{ cm}^{-2}$ ), so we attributed this value to each density. In *Tab. 1* we present also the mobilities calculated with the classical formula  $\mu = \frac{1}{n(V)e\rho_{xx}^0}$ , where  $\rho_{xx}^0$  is the longitudinal resistance at the considered gate potential at  $B = 0T$ .

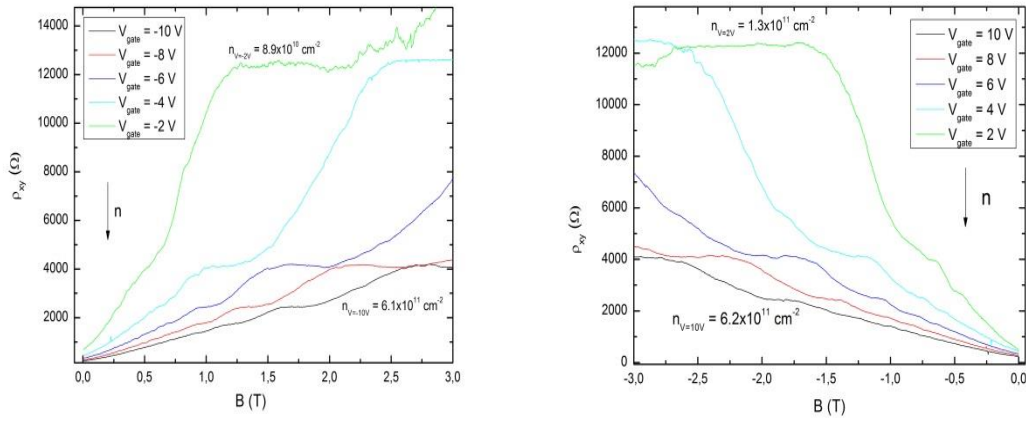


**Figure 26.** Left and right are reported both the Hall resistivities (at different gate voltages) for positive and negative magnetic field. As it is shown by the arrow, charge carrier density increases with the increasing of  $V_g$ .

$V_{\text{gate}} \text{ (V)}$	$n \pm \delta n \text{ (cm}^{-2}\text{)}$	$\mu \text{ (cm}^2 \text{ V}^{-1} \text{ s}^{-1}\text{)}$
-10	$6.023 \cdot 10^{11} \pm 6 \cdot 10^9$	56945
-8	$4.372 \cdot 10^{11} \pm 6 \cdot 10^9$	62621
-6	$3.576 \cdot 10^{11} \pm 6 \cdot 10^9$	62342
-4	$2.136 \cdot 10^{11} \pm 6 \cdot 10^9$	76703
-2	$8.867 \cdot 10^{10} \pm 6 \cdot 10^9$	88999
0	$3.574 \cdot 10^{10} \pm 6 \cdot 10^9$	90589
2	$1.257 \cdot 10^{11} \pm 6 \cdot 10^9$	84455
4	$2.299 \cdot 10^{11} \pm 6 \cdot 10^9$	67879

6	$3.169 \cdot 10^{11} \pm 6 \cdot 10^9$	65440
8	$4.373 \cdot 10^{11} \pm 6 \cdot 10^9$	57790
10	$6.179 \cdot 10^{11} \pm 6 \cdot 10^9$	47650

**Tab. 1** Charge carriers' density calculated from the linear fit of Hall resistances.

Subsequently, with data obtained from the transport measurements (used to obtain the Dirac peak) we calculated the mobility  $\mu$  (Hall mobility) using the standard formula  $\mu = \frac{1}{n(V)e\rho_{xx}^{\square}}$ , where  $\rho_{xx}^{\square}$  is the squared (at zero field) longitudinal resistivity. This  $n(V)$  instead is the carrier density obtained with  $n(V) = \alpha(V_g - V_{CNP})$ :  $\alpha$  is the slope obtained from the linear fit of *Figure 27. (right)* and, from the theory presented in [17], it has the form  $\alpha = \frac{C}{eA}$  where  $C$  is the capacity of the system,  $e$  the electric charge and  $A = L \times W$  the surface of the capacitor. Within this model, mobility tends to diverge at lower densities and should be  $\infty$  at  $V_g \sim 0V$ . The data calculated and the fit are plotted in *Figure 27. (left)*.

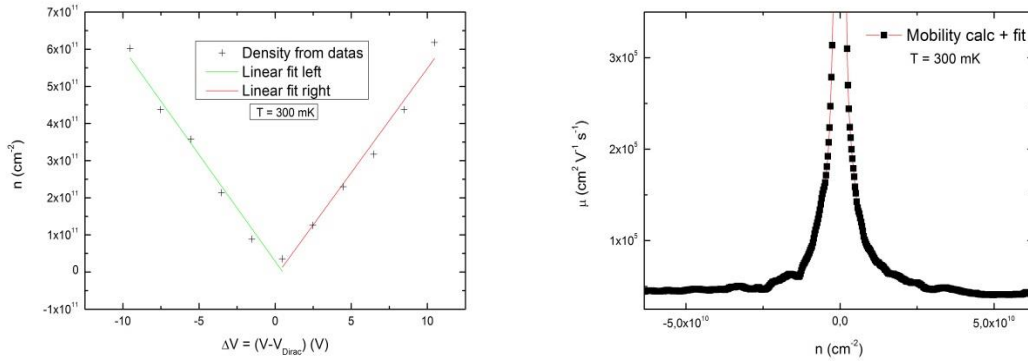


**Figure 27.** On the left it are plotted the density values vs the potential. As it can be seen, it increases with the increasing of the density. It is plotted the linear fit of the positive and the negative component.

The right figure presents the mobility calculated as explained in the text with its nonlinear fit.

While measuring, we noted that both the Hall and the longitudinal resistances were not very clear, clean from noise or precise as in good graphene's samples, even if the Dirac peak had a really high peak-value and a small width. An example is the plot in *Figure 28*. of the Halls and the Shubnikov-de Haas at  $V_g = 4V$ . As it is possible to see, the Hall measurement presents plateaus defined at  $B < 1T$ ; after, the behavior is not the expected. The longitudinal resistances are not so good and the peaks not always correspond to the Hall's plateaus. There are a lot of theories that tries to explain this behavior. Sometimes there are problems with contact alignments or inhomogeneity in the sample. For these reasons, we studied our sample with interesting theories, in order to verify the connection between its behavior and the theories that consider alignments problems and inhomogeneities of graphene-based samples.

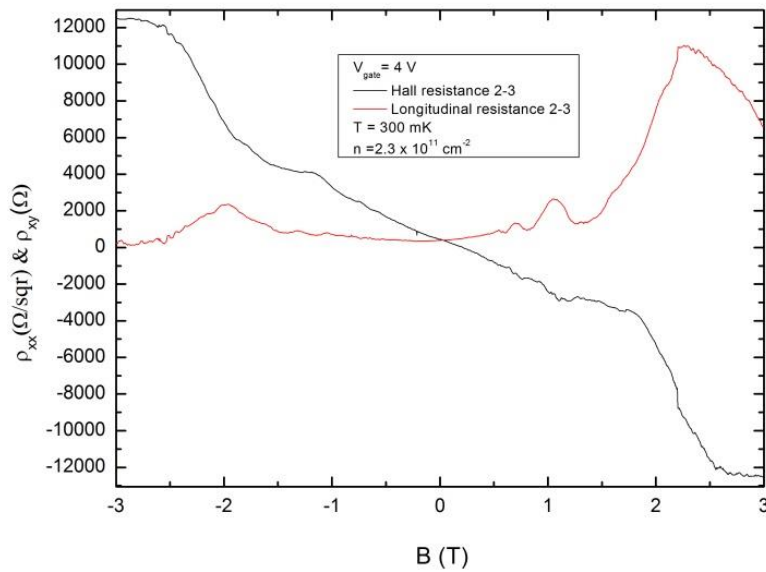


**Figure 28.** Plot of the longitudinal (red) and transverse (black) resistivity for  $V_g = 4V$  for positive and negative magnetic fields.

## 6.2 Weak Localization/Weak AntiLocalization

After the first measurements we decided to follow the idea, used previously in other samples [12], to investigate the Weak Localization and the Weak Anti-Localization presence in the one we were analyzing. This phenomena appear at low magnetic fields: in this case the measurements were done at  $V_g = 0V$  and at  $V_g = 2V$ , slowly varying the magnetic field between  $-0.2 < B < 0.2$ . These effects are really weak and could appear at the same time in the longitudinal resistivity measurement. In particular for the WL we should see an increase of the resistivity while lowering the magnetic field and for the WAL a decrease of the resistivity while decreasing the field. One of the measurements we acquired is plotted in *Figure 29*. From this picture it is possible to see that there is only a small probable trace of WL, but it is something not sure. So we accepted the idea that this wasn't an evidence of the presence of the effects. This behavior is not so easy to be explained; there are a lot of theoretical reasons that could explain the origin of both the effects and, when they doesn't appear, it is very difficult or impossible to understand the real reason.

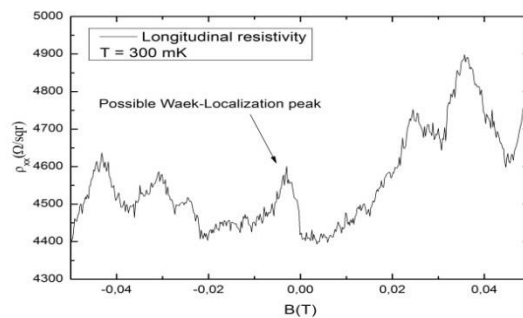


**Figure 29.** Plot of the longitudinal resistivity for a small range of variation of the magnetic field. This measurements has an higher resolution in B respect to the previous one because we were looking for WL/WAL. As indicated by the arrow, there should be a possible presence of WL but it is something really small or not so evident.

### 6.3 Solving the inhomogeneity

The first thing we tried to do is to see if it was possible to improve the quality of the measurements. In each case (for each  $V_g$ ) we registered data for positive and negative magnetic field, also with  $|B|$  increasing and decreasing. For the longitudinal and Hall resistances we applied respectively the formulas:

$$R_{long, symm} = \frac{R_{xx}^{incr} + R_{xx}^{decr}}{2} \quad (23) \quad \text{and} \quad R_{Hall, antisymm} = \frac{R_{xy}^{incr} - R_{xy}^{decr}}{2} \quad (24).$$

However the result of this symmetrization/antisymmetrization is not satisfying (Figure 30.), since the plots were worse than before. A peculiar thing that we could note was a type of hysteresis of the system while going back to  $B = 0T$ .

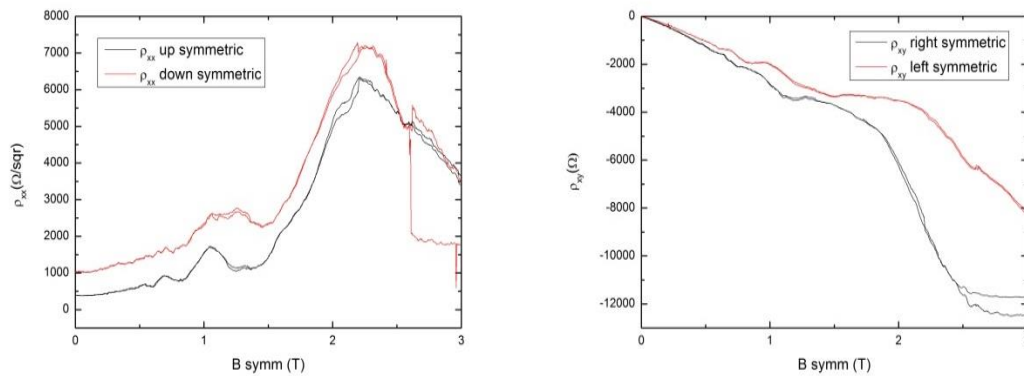


**Figure 30.** Plot of the longitudinal (left) and Hall (right) resistivities symmetrized (the Hall properly are anti-symmetrized). Each of them is double because one is for the magnetic field increasing and the other decreasing. There is no evidence of a gain of their quality.

How it is explained in the paragraph before, for each  $V_g$  we calculated the density of carries by the linear fit of the Hall resistances. Thanks to the device's contacts distribution, we could measure at the same time two different transverse resistances between contact 2-5 (B-F) (called *left*) and 3-6 (C-E) (called *right*): these gave two different values of  $n$ , called  $n^{left}$  and  $n^{right}$ . Another thing that we noted was that the longitudinal and transverse resistivities were not symmetric with the magnetic field. Then we tried to apply a theory to verify if there should be an inversion symmetry in the resistivities. This behavior was previously observed in mesoscopic Hall bars in semiconductor 2D electron gases and can be attributed to inhomogeneity of the same sample. [12] The inhomogeneity leads to non-zero gradients in the carriers' density along the bar: this is known as a theory of Karmakar et al..

Our group applied this theory a few years ago to an inhomogeneous sample (where  $\rho_{xx}^{t,b}(B) \cong \rho_{xx}^{b,t}(-B)$ ) achieving good results [12]; so I tried to use the same one to understand the behavior of BNSD1S3HB2. The magnetic field in this type of sample has to induce a non-uniform accumulation of charge carriers at the boundaries, which causes inhomogeneity of the current density; the resistivities measured should be written in this way:

$$\rho_{xx}^{t,b} = \left( \rho_{xx} \pm \rho_{xy} \beta \frac{W}{2} \right) = \frac{W}{L} R_{xx}^{t,b} \quad (25)$$

$$\rho_{xy}^{l,r} = \rho_{xy} \left( 1 \pm \beta \frac{L}{2} \right) = R_{xx}^{l,r} \quad (26)$$

with  $\beta$ : phenomenological parameter that depends on the temperature and on the magnetic field,  $t$ =top is the longitudinal resistivity between contacts 2-3 and  $b$ =bottom between contacts 5-6. From these relations it is simply to deduce that

$$\Delta R_{xx} = R_{xx}^t - R_{xx}^b = R_{xy}^r - R_{xy}^l = \Delta R_{xy} = \Delta R \quad (27)$$

if the theory is valid, independently from the magnetic field. In particular, we obtain  $\Delta R = 0$  for homogeneous samples and  $\Delta R \neq 0$  for inhomogeneous samples. The quantity  $\beta L$  is really important: it represents the percentage quantity that expresses the level of inhomogeneity and should be calculated also independently by the relation  $\beta L = ((n^l - n^r)/n^l + n^r)/2$  (28).

If all these conditions are satisfied, thanks to the relation

$$\rho_{xx}(B) = \frac{[\rho_{xx}^t(B) + \rho_{xx}^b(B)]}{2} = \frac{[\rho_{xx}^{t,b}(B) + \rho_{xx}^{b,t}(-B)]}{2} \quad (29)$$

it is possible to calculate the “real” longitudinal resistivity. The same thing shouldn't be done with the Hall resistivities because of the density's inhomogeneities between the left and the right part.

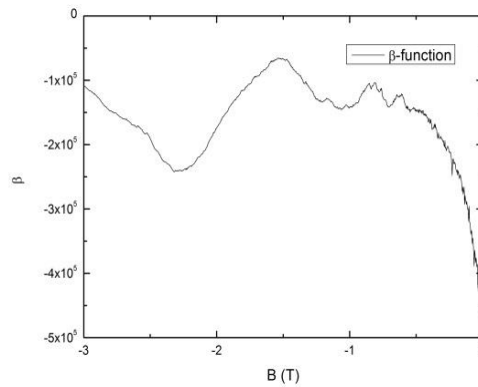


**Figure 31.**  $\beta$  parameter obtained inverting the relation to the relations (25) and (26). It is not a constant, as expected from the theory.

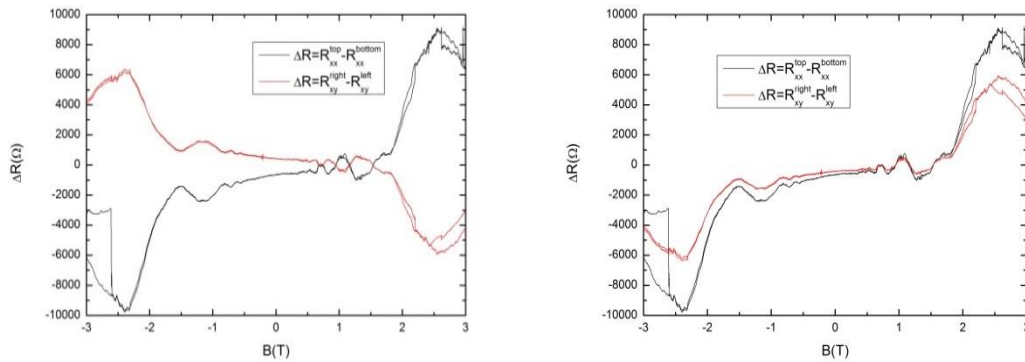


**Figure 32.** Plots of the relation (27): on the left without corrections and on the right the plot with the sign of the Hall resistivity inverted. As it can be seen, the red and black lines does not coincide; the theory is not verified.

Elaborating data acquired for each  $V_g$ , the behavior supposed by this model was not successfully satisfied: relation (25), (26) and (27) were not fully consistent with our data, as can be seen in *Figure 32.*, and the parameter  $\beta$  hasn't got the form expected, as supposed to be (see *Figure 31.*).

Thinking on these results, Karmakar's theory doesn't help to understand the behavior of our sample and doesn't suggest a possible cause that originates it. In particular, as was the aim of this paragraph, we were not able to extract a good Hall resistivity and a good longitudinal resistivity from the data acquired by our sample, and we couldn't know the percentage of inhomogeneity present in it using Karmakar's method.

## 7. Conclusions

Graphene is one of the most interesting material to be investigated. Its unique electronic properties offer the chance to verify a lot of theories and to understand quantum properties that at the moment are not completely understood. For my personal interest, the work in this field implies a strong importance of the experimental part. It gave me the possibility to improve my theoretical and practical skills and learn experimental techniques, only studied theoretically in my Master career.

The measurements we performed turned out to be a useful tool to face our issues because they gave us the opportunity to fully characterize the samples. In my three months at the Low Temperature Laboratory in Salamanca I worked a lot, first of all for improving my ability to produce graphene and h-BN samples with the mechanical exfoliation technique and secondly to learn how to perform magnetotransport measurements. In Pavia, instead, I understood how to perform Raman measurements with the Raman spectrometer we have there. I think that the understanding of the importance of these techniques and how to manage instruments is a good success of my thesis. Furthermore, experimental results are really important: I wasn't so lucky to find something new but what I measured is really interesting, both for a comparison with the theoretical knowledge (that I built during my university courses) and for data analysis' methods that I learned.

Talking about the experimental techniques, Raman spectroscopy is something incredible: it is sensible to the type of material, is the fingerprint of each of them. So it gives the possibility to understand what we are measuring and its degree of purity because it is sensible to the doping level and to the impurities and defects' concentration. We principally performed Raman measurements in order to understand

both the number of graphene and h-BN's layers, that cover the substrate on which they are deposited, and their quality. This is really important also because there is the possibility to predict the behavior of the sample studied. At the same time we employed magnetotransport experimental technique: as Raman spectroscopy, we used it for a characterization intent. We had an idea of its electronic characteristics and we look for new interesting behaviors. The presence of impurities, defects or inhomogeneities is something expected. We think that a strong affection by these ones causes what happened to our sample: its behavior seems to depend on inhomogeneities of carriers' density, but we are not sure. The sample worked properly but measurements were not as good as expected. From all this work I understood that these techniques are capable to provide information for the electronic characterization but we were not able to characterize sample's inhomogeneity with the theories we know.

All the work I've done was really interesting: it led me to think about my future, about the possibility to go on working with graphene during a PhD. The work with Enrique Diez was stimulating, I had the possibility to be independent in my organization and I learned a lot of theoretical and experimental things. Working in a laboratory is really interesting and inspiring: you can understand better what you studied during the courses, you can work independently with instrument and you can make errors. This last one is the most challenging part because the challenge is to understand why you made a mistake or why something doesn't work properly or, analyzing data, why something doesn't give the results expected. I hope that there will be the possibility to go on with my work in Salamanca, with Enrique, facing again with graphene's issues.

# Bibliography

- [1] A. H. Castro Neto et al., Rev. Mod. Phys. **81**, 109-162 (2009)
- [2] M. I. Katsnelson, MaterialsToday, **10**, 1-2 (2007)
- [3] C. R. Dean et al., Nature Nanotechnology
- [4] A. C. Ferrari, Solid State Communications, **143**, 47-57 (2007)
- [5] P. Blake et al., Appl. Phys. Lett. **91**,063124 (2007)
- [6] A. C. Ferrari et al., PRL **97**, 187401 (2006)
- [7] R. V. Gorbachev et al., Small, **7**, 465-468 (2011)
- [8] S. Reich et al., Physical Review B, **71**, 205201 (2005)
- [9] R. Rao et al., ACS Nano, **5**, No. 3, 1594-1599 (2011)
- [10] C. Cobaleda et al., Phys. Status Solidi C **9**, No. 6, 1411-1414 (2012)
- [11] E. Peled et al., Phys. Review B **69**, 241305(R) (2004)
- [12] C. Cobaleda et al., Physica E **44**, 530-533 (2011)
- [13] B. Jeckelmann and B. Jeanneret, Rep. Prog. Phys. **64**, 1603-1655 (2011)
- [14] Andrei G. F. Garcia et al., Nano Lett. **12**, 4449-4454 (2012)
- [15] C. R. Dean et al., Nature Physics **7**, 693-696 (2011)

- [16] E. Diez et al., Appl. Phys. Lett. **88**, 052107 (2006)
- [17] S. Kim et al., Appl. Phys. Lett. **94**, 62017 (2009)
- [18] J. D. Lejarreta et al., J. Phys. A:Math. Theor. **46**, 155304 (2013)
- [19] A. K. Geim, Science **324**, No. 5934,1530-1534 (2009)
- [20] G. Grosso and G. Pastori Parravicini, Solid State Physics, Academic Press, 152 (2000)
- [21] D. Cammi, L'effetto Hall Quantistico, 2008
- [22] M. Amado Montenero, Electronic structure and transport properties in graphene and other nanoscopic systems, 2011
- [23] L. C. Andreani, Fisica dei Semiconduttori, 1999
- [24] N. W. Ashcroft and N. D. Mermin, Solid State Physics, Hearcourt College Publishers, 1976
- [25] P. Y. Yu and M. Cardona, Fundamentals of Semiconductors, Springer, 2010
- [26] S. Datta, Electronic transport in mesoscopic Systems, Cambridge University Press, 1995
- [27] S. Pezzini, Magnetotrasporto in grafene: uno studio sperimentale, 2010